



## UvA-DARE (Digital Academic Repository)

### Some applications of magnetic resonance imaging in fluid mechanics: Complex flows and complex fluids

Bonn, D.; Rodts, S.; Groenink, M.; Rafai, S.; Shahidzadeh-Bonn, N.; Coussot, P.

**DOI**

[10.1146/annurev.fluid.40.111406.102211](https://doi.org/10.1146/annurev.fluid.40.111406.102211)

**Publication date**

2008

**Published in**

Annual Review of Fluid Mechanics

[Link to publication](#)

**Citation for published version (APA):**

Bonn, D., Rodts, S., Groenink, M., Rafai, S., Shahidzadeh-Bonn, N., & Coussot, P. (2008). Some applications of magnetic resonance imaging in fluid mechanics: Complex flows and complex fluids. *Annual Review of Fluid Mechanics*, 40, 209-233. <https://doi.org/10.1146/annurev.fluid.40.111406.102211>

**General rights**

It is not permitted to download or to forward/distribute the text or part of it without the consent of the author(s) and/or copyright holder(s), other than for strictly personal, individual use, unless the work is under an open content license (like Creative Commons).

**Disclaimer/Complaints regulations**

If you believe that digital publication of certain material infringes any of your rights or (privacy) interests, please let the Library know, stating your reasons. In case of a legitimate complaint, the Library will make the material inaccessible and/or remove it from the website. Please Ask the Library: <https://uba.uva.nl/en/contact>, or a letter to: Library of the University of Amsterdam, Secretariat, Singel 425, 1012 WP Amsterdam, The Netherlands. You will be contacted as soon as possible.

# Some Applications of Magnetic Resonance Imaging in Fluid Mechanics: Complex Flows and Complex Fluids

Daniel Bonn,<sup>1,2</sup> Stephane Rodts,<sup>3</sup>  
Maarten Groenink,<sup>4</sup> Salima Rafai,<sup>2</sup>  
Noushine Shahidzadeh-Bonn,<sup>2,3</sup>  
and Philippe Coussot<sup>3</sup>

<sup>1</sup>Laboratoire de Physique Statistique, Ecole Normale Supérieure,  
75231 Paris Cedex 05, France; email: Daniel.Bonn@lps.ens.fr

<sup>2</sup>van der Waals-Zeeman Institute, University of Amsterdam, 1018XE Amsterdam,  
The Netherlands

<sup>3</sup>Laboratoire Navier, Université Paris-Est, 77420 Champs sur Marne, France

<sup>4</sup>Department of Cardiology and Radiology, Academic Medical Center,  
1105 AZ Amsterdam, The Netherlands

Annu. Rev. Fluid Mech. 2008. 40:209–33

The *Annual Review of Fluid Mechanics* is online at  
fluid.annualreviews.org

This article's doi:  
10.1146/annurev.fluid.40.111406.102211

Copyright © 2008 by Annual Reviews.  
All rights reserved

0066-4189/08/0115-0209\$20.00

## Key Words

MRI flow measurement, multiphase flows, complex fluids, granular matter, blood flow

## Abstract

The review deals with applications of magnetic resonance imaging (MRI) techniques to study flow. We first briefly discuss the principles of flow measurement by MRI and give examples of some applications, such as multiphase flows, the MRI rheology of complex fluid flows, and blood flows in the human body.

## 1. INTRODUCTION

Because most illustrations of the magnetic resonance imaging (MRI) technique occur in the medical field, many believe that MRI is a technique that mainly provides nice colorful 3D pictures. In reality, proton MRI, which is the basis of the vast majority of MRI measurements, can be used to measure a wide range of different parameters within a sample, such as hydrogen density, relaxation time, velocity, acceleration, and diffusion coefficients (Callaghan 1999). One can also obtain more detailed chemical information about molecules by using some specialized MRI facilities, mixing nuclear magnetic resonance (NMR) spectroscopy and MRI techniques. Therefore, when one wants to get a picture of a sample, MRI already proposes many different contrast sources, and also the measured information can be much more than a simple color.

Although NMR was originally developed in the field of physics, most of its imaging-related applications presently are in the medical field. Indeed, most modern hospitals are equipped with several MRI scanners that are mostly used for diagnostic purposes. This application of NMR has led to the development of commercially available MRI scanners with high magnetic fields and user-friendly interfaces that are, among many other things, perfectly suited to, and used for, measuring 3D flow fields.

Nowadays, simply typing “MRI and flow” in the Web of Science results in over 6300 hits with, perhaps surprisingly, only a small fraction (on the order of 100) for physics and engineering. Most MRI research-type flow measurements are again done in medicine, with cardiology representing the largest part. Over the past few years, however, there has been a renewed interest in the fields of physics and engineering in using MRI for flow measurements in a number of situations in which other techniques usually fail.

When comparing MRI with other standard imaging techniques such as X-ray tomography, one may question if the spatial resolution on MRI pictures is not too limited. Because of signal-to-noise constraints, pixels usually cannot be much smaller than one-hundredth of the sample size. On some microimaging devices, one can obtain 10- $\mu\text{m}$  resolution when working on samples a few millimeters in size; however, this is still rather far away from the 1- $\mu\text{m}$  resolution that can be achieved now with many X-ray tomographic devices.

Surprisingly, MRI motion sensitivity is much more accurate because imaging and motion measurement techniques are not subject to the same constraints. Even on big MRI facilities, in which the spatial resolution cannot be better than 1 mm, sample displacements of less than 1  $\mu\text{m}$  and velocities as small as 10  $\mu\text{m s}^{-1}$  can be measured. This accuracy for flow measurement, as well as the unique possibility of working on opaque or heterogeneous systems, makes MRI particularly well suited for fluid mechanics research.

Previous reviews (Callaghan 1999, Fukushima 1999, Stapf & Han 2006) already have compiled, in a quasi-exhaustive way, the state of the art of all the possibilities that MRI offers in different fields, such as chemical engineering, fluid mechanics, and fluid transport in porous media. However, in spite of all the possibilities for the use of MRI, the gap between what MRI can potentially do and what MRI methods are routinely used for in fluid mechanics is still large.

Therefore, in the following sections, we do not review all the possibilities that MRI offers, but instead we highlight the state-of-the-art use of MRI in some fluid mechanical problems. We mainly consider rapid flows because these have recently become much more accessible experimentally and much of the recent progress has come from this area, not only in physics and engineering, but also in medicine. We present two topics from classical fluid mechanics (multiphase flow and transport in porous media) as an example, but mainly focus on recent and rather exciting results in the MRI rheology of complex fluids, in addition to exploring the current status of MRI flow measurements in medicine, notably cardiology. To set the stage, we first briefly review the principles of MRI and MRI velocimetry.

## 2. OVERVIEW OF NUCLEAR MAGNETIC RESONANCE AND MAGNETIC RESONANCE IMAGING

### 2.1. Basics

MRI (Callaghan 1999) is one of the NMR techniques. It makes use of the spin properties of atomic nuclei to get spatially resolved information about the structure and dynamics inside a sample. Any detailed description of NMR phenomenon requires the use of quantum mechanics. However, an approximate description by the means of classical concepts is often sufficient to derive most MRI principles, and we use this approach here.

We consider hereafter the so-called proton NMR, the NMR of hydrogen nuclei, for which the classical description turns out to be quite accurate. Because of their spin properties, any small group of hydrogen nuclei (which does not depend on their belonging to the same molecule) may develop, under appropriate conditions, a nonzero magnetic dipole  $\vec{M}$ : the magnetization vector. When immersed in a sufficiently strong magnetic field  $\vec{B}_0 = B_0 \vec{e}_z$  (order of magnitude: 1 Tesla),  $\vec{M}$  exhibits a threefold behavior depicted schematically in **Figure 1**.

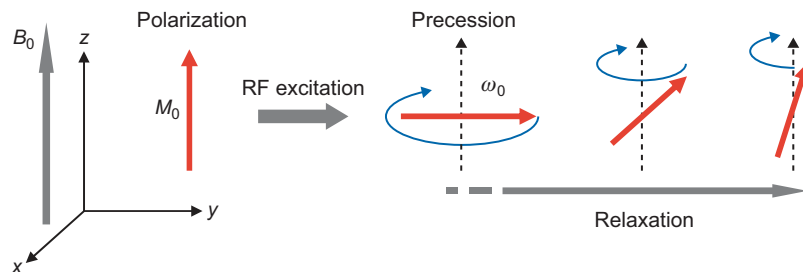


**Figure 1**

The threefold behavior of spin magnetization in nuclear magnetic resonance. From left to right, polarization in a strong static magnetic field, and precession and relaxation in out-of-equilibrium situations. RF, radio frequency.

1. *Polarization.* At rest,  $\vec{M}$  reaches a stable equilibrium value  $\vec{M}_0$ :

$$\vec{M}_0 = \frac{\gamma^2 \hbar^2}{kT} \vec{B}_0.$$

The constant  $\gamma$  is the gyromagnetic ratio of hydrogen nuclei.

2. *Precession.*  $\vec{M}$  can be tilted away from its equilibrium value when irradiated by a radio-frequency magnetic field at proper frequency  $\omega_0 = \gamma B_0$ , corresponding to the so-called Larmor frequency (approximately 40 MHz at 1T). This is a resonant process, and experimental setting of this frequency should be quite accurate. Just after tilting,  $\vec{M}$  does not come back at once to its equilibrium value  $\vec{M}_0$  but precesses some time around  $\vec{B}_0$  at frequency  $\omega_0$ :

$$\frac{d\vec{M}}{dt} = \gamma \vec{M} \wedge \vec{B}_0.$$

A simple radio-frequency antenna settled close enough to the sample can detect precession in amplitude and phase. Only transverse component  $M_x$  and  $M_y$  are actually measured, giving rise to the so-called complex NMR signal:

$$S(t) = M_x(t) + i M_y(t).$$

3. *Relaxation.* While precessing,  $\vec{M}$  progressively gets closer to  $\vec{M}_0$ . Relaxation in fluids usually involves two independent first-order processes: (a) longitudinal relaxation, with characteristic time  $T_1$ , corresponding to  $M_z$ 's returning to  $M_0$  value, and (b) transverse relaxation, corresponding to the vanishing of both  $M_x$  and  $M_y$  values, with characteristic time  $T_2$ . For instance, the NMR signal emitted after a full tilting of  $\vec{M}_0$  in  $x$  direction reads

$$S(t) = M_0 \exp\left(-i\omega_0 t - \frac{t}{T_2}\right).$$

## 2.2. The MRI Facility

An MRI facility (shown schematically in **Figure 2**) usually comprises three different parts. (a) The magnet creates the constant and homogeneous magnetic field  $\vec{B}_0$  inside the sample. Popular at the moment are superconducting systems, which provide the best field stability. (b) The radio-frequency coil, which surrounds the sample area, often works both as an emitter and a receptor for radio-frequency fields and alternatively initiates and detects precession motion during experiments. The magnet and radio-frequency coil are actually part of any NMR spectrometer. (c) Gradient coils locate and detect sample motions throughout space. They produce at will a controlled inhomogeneous static magnetic field inside the sample, which superimposes on  $\vec{B}_0$  and results in a homogeneous space gradient for Larmor frequency:

$$\omega_0 = \gamma B_0 \rightarrow \gamma(B_0 + \vec{G} \cdot \vec{r}).$$

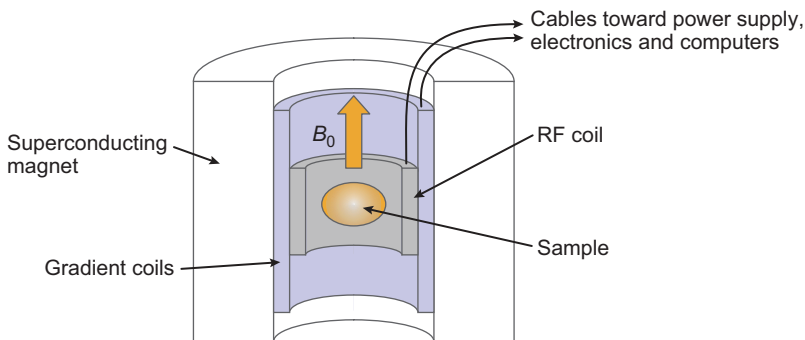


**Figure 2**  
Basic structure of usual magnetic resonance imaging facilities. RF, radio frequency.

Therefore, no probe needs to be inserted inside the sample. As long as the magnetic field does not affect the sample behavior, MRI can be seen as a nonperturbative technique.

### 2.3. MRI Sequence

To get any information about the sample, MRI performs a series of short excitation-measurement cycles, called sequences, on the spin system. Although an extensive description of the methodology used for fluid mechanic purposes is out of the scope of this article, we summarize the philosophy of most involved sequences through the example shown in **Figure 3**.

The sequence starts with a radio-frequency emission that puts the magnetization out of equilibrium. For a global excitation of the whole sample, the excitation frequency should be  $\omega_0$ . However, this frequency can also be shifted to another value,  $\omega_1$ , and associated with a gradient  $\vec{G}_0$ , to create a so-called space-selective excitation: Because of the resonant characteristics of the excitation process, only those nuclei located close to the plane defined by  $\omega_1 = \omega_0 + \gamma \vec{G}_0 \cdot \vec{r}$  effectively start to precess. Actually, any simple-shaped restricted part of the sample can be selected through this trick.

Then, a time-dependent gradient  $\vec{G}(t)$  is applied. By solving precession-relaxation equations, the general form of the NMR signal emitted by a piece of sample

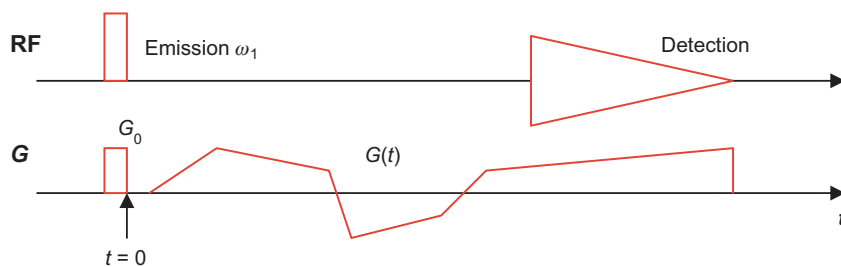


**Figure 3**  
Schematic illustration of a magnetic resonance imaging sequence. RF, radio frequency.

undergoing a trajectory  $\vec{r}(t)$  and with transverse relaxation time  $T_2$  reads

$$S(t) = m_0 \exp\left(-i\omega_0 t - i\gamma \int_0^t \vec{G}(t') \cdot \vec{r}(t') dt' - \frac{t}{T_2}\right).$$

The NMR signal is recorded when needed. This elementary signal depends on many pieces of information. The excited magnetization  $m_0$  at  $t = 0$  is usually proportional to the hydrogen density inside the sample.  $T_2$  loss in signal amplitude often depends on local physical chemistry. Eventually, the integral term involving  $\vec{G}(t)$  and  $\vec{r}(t)$  can be expanded as a Taylor series:

$$\begin{aligned} \int_0^t \vec{G}(t') \cdot \vec{r}(t') dt' &= \vec{r}(t=0) \int_0^t \vec{G}(t') dt' \\ &+ \frac{d\vec{r}}{dt}(t=0) \int_0^t t \vec{G}(t') dt' + \frac{1}{2} \frac{d^2\vec{r}}{dt^2}(t=0) \int_0^t t^2 \vec{G}(t') dt' + \dots \end{aligned}$$

Depending on the exact shape of  $\vec{G}(t)$ , one can make these different integral terms independent and thus track different aspects of the trajectory, such as position, velocity, and acceleration.

In a flowing fluid, each part of the sample undergoes its own history during the sequence time, and the global NMR signal is the sum of thousands of such elementary signals. The main job for the MRI scientist is to design a series of sequences in such a way to make it possible, through further data processing, to sort all desired information.

When requirements about the amount and accuracy of information are small, one single sequence execution can sometimes be sufficient: The measurement lasts a few milliseconds and is said to be a snapshot. When full 3D information is required with high accuracy, several thousands of successive sequences may be needed: The NMR measurement process can last up to a few hours and is only suited for static or statistically static situations.

MRI measurements are not necessarily always 3D pictures. They can also be simply 2D or 1D projections of all or some part of the sample. For the purposes of MRI velocimetry, which is the subject of this article, the results may even take the form of simple curves, e.g., a velocity component versus a space coordinate.

## 2.4. MRI Velocimetry: Trends in Methodology

The application of MRI techniques to quantify flow dates back at least to 1959, well before the potential of MRI was discovered, and was clinically implemented in the early 1980s (Singer 1959, Singer & Crooks 1983). The velocity inside a flowing fluid may be probed in various ways. The first technique used was time of flight, also called bolus, based on the NMR excitation of a restricted part of the fluid and tracking its position throughout time (see, e.g., Merbolt et al. 1986). The spin-tagging technique (Zerhouni et al. 1988) is based on the same idea but tracks a more complex magnetic pattern drawn on the whole fluid and allows a spatially resolved description of the flow. A beautiful example of this method is presented by Moser (2000), who observed Taylor-Couette flow in a Couette rheometer. **Figure 4** shows another example, in

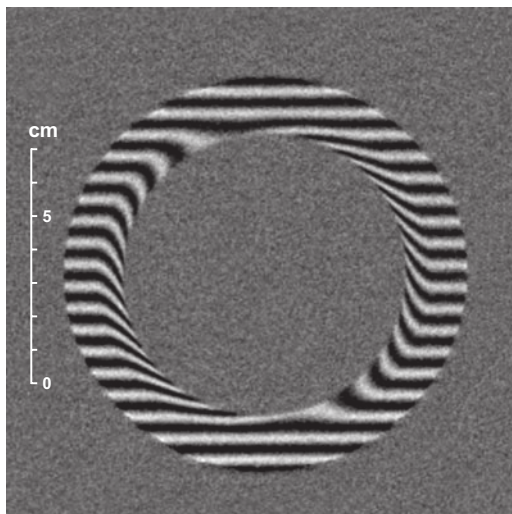


**Figure 4**

A 2D image of a flowing clay suspension (bentonite) in a Couette cell, showing the deformation of virtual lines in the sample. This specific example shows shear localization; i.e., part of the material closest to the moving inner cylinder flows, whereas the other part does not.

which the bright lines correspond to tagged spins that were tagged on straight lines at time zero; the deformation of the lines owing to the flow is clearly visible. One drawback of the spin-tagging technique is that flow measurement requires complex image processing. In addition, the space density of original information is often sparse, so both the spatial resolution and velocity accuracy suffer strong limitations.

More accurate techniques are phase-shift or phase-contrast velocity mapping (Dumoulin et al. 1989, Fukushima 1999, Pelc et al 1991). These techniques make use of the above-mentioned flow-induced changes in signal phase. In such measurements, a phase map of the NMR signal is drawn throughout space. Velocity information is obtained by comparing in each single pixel the measured phase with the zero phase of a flow-compensated reference phase map. Because one can get detailed information about flow inside each pixel, phase-shift methods offer the best spatial resolution currently. They are also the most accurate, and velocity as small as a few tens of micrometers per second can be measured.

The phase-shift technique has been validated extensively, both in and ex vivo (Hundley et al. 1995), and applications of this technique are plentiful (see Stapf & Han 2006). As an example, **Figure 5** shows the results of Rodts et al. (2004), who measured a full 3D velocity map for a visco-elastic fluid (carbopol) moving inside a small model of a concrete blender.

Other techniques include those with exogenous and endogenous (spin-labeling) tracer methods, which are used in functional brain imaging (Petrella & Provenzale 2000). We do not discuss these techniques further here.

### 3. MULTIPHASE FLOW AND FLOW IN POROUS MEDIA

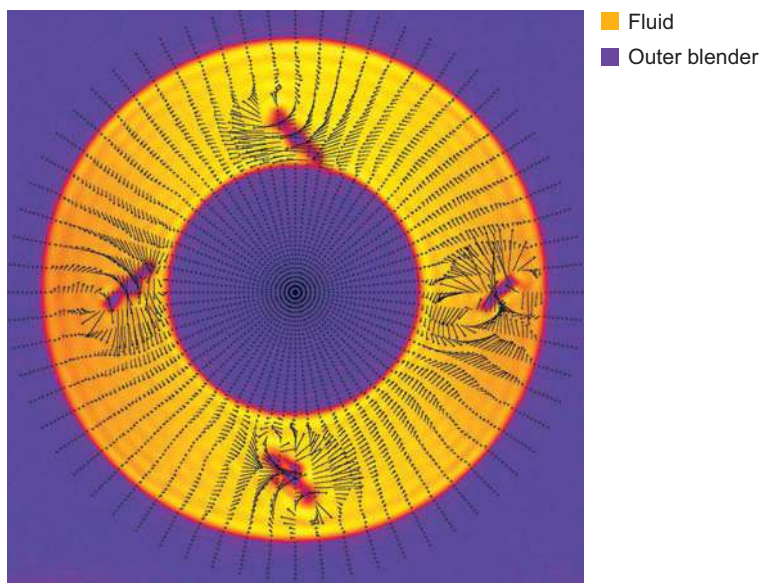
#### 3.1. Multiphase Flow

Multiphase flow is of huge importance for industrial applications; pertinent examples include heat exchangers and oil recovery. The main problem engineers are facing in



**Figure 5**

A 2D section of a 3D velocity map in a carbopol gel moving inside the annular container of a small model of a concrete blender (phase-shift magnetic resonance imaging measurements). The fluid is shown in orange; the outer part of the blender is shown in violet. Only in-plane components of the velocity field are shown.



these applications is that the distribution of the phases in the flow has a great impact on the flow properties (for instance, the pressure drop), but the fluid distribution in general is not known. Although in principle MRI is a powerful tool to use to access both velocity and concentration profiles in a flowing system, few MRI experiments on multiphase flow exist (Götz & Zick 2003, Le Gall et al. 2001, Muller et al. 2007). Here we consider some measurements done by S. Rafai, F. Bertrand & D. Bonn (unpublished manuscript), who used a Couette cell inside a vertical MRI apparatus to characterize the fluid distribution in the flow of an oil-water system. **Figure 6** shows

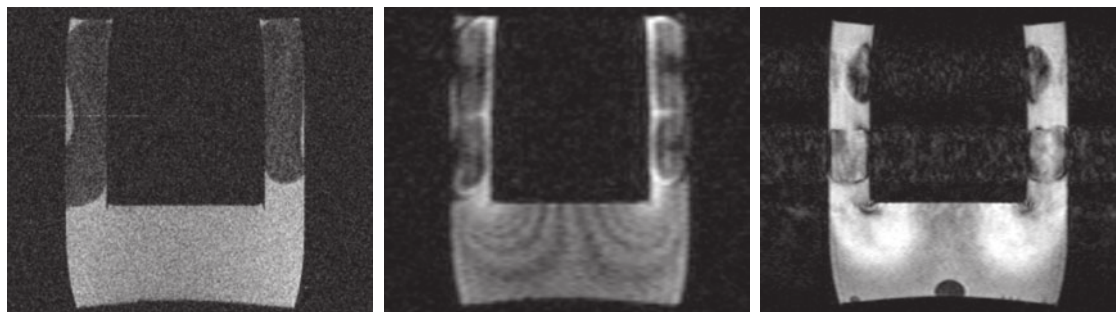


**Figure 6**

Oil and water mixing in a Couette cell rheometer, showing the evolution of the sample inside a 2D cross section along the axis of the cell. The imaging sequence was chosen so that water appears in white, and oil in black. Starting from a fully demixed situation (*left panel*), a progressive increase of the water signal in the top region of the cell is observed as mixing goes on; this is one of the clues for the emulsification process. In the far-right panel, imaging artifacts due to fluid motion can be observed; these may be removed by a proper choice of parameters for the MRI measurements.

the results of the MRI measurements of the fluid distributions; at rest oil and water are completely demixed. For intermediate velocities, partial mixing occurs, which is most likely initiated by Taylor-Couette vortices that lead to a flow instability. Finally, at the highest speeds, the material becomes homogeneous owing to the turbulence inside the cell (the Reynolds number becomes on the order of 500): The oil phase is finely dispersed as droplets within the water phase, and an emulsion has formed. Measurements show that the flow resistance of the emulsion can be  $10^3$  times as large as that of the demixed oil-water system. This clearly demonstrates the necessity of measuring the fluid distribution under flow; in fact these experiments were inspired by observations of a huge increase in flow resistance in oil recovery pipes, in which oil, water, and gas flow out simultaneously, and under some specific conditions a strong increase in apparent viscosity is observed (Hall 1997).

### 3.2. Flow in Porous Media

An important application of MRI is that of fluid transport in porous media, again a significant domain in industrial engineering. Mantle & Sederman (2003) have recently reviewed gas/liquid and liquid/liquid flows in porous media. Traditionally, researchers have used techniques such as X-ray tomography or gamma-ray densitometry for this application. However, the errors involved in such measurements are rather large because in general both the porous medium and the liquid absorb some of the radiation. In MRI, this is not a problem, and presently one can readily obtain quantitative 3D images, for instance, of the water distribution inside a rock or a piece of concrete. In more recent years, attention has shifted somewhat to studies of the dynamics of liquid transport in porous media, such as imbibition, and the drying and drainage of water in porous media. Recently, researchers have focused on the fundamental understanding of the relation between the flows and the properties of the porous medium.

As a mere example of the vast literature that exists on this subject (for reviews, see Callaghan 1999, Fukushima 1999, Stapf & Han 2006), we discuss Shahidzadeh-Bonn et al.'s (2004) recent experiment on the dynamics of water drainage from model porous media with different wetting properties. They studied the effect of wetting on the dynamic gravity drainage (two-phase flow) in well-controlled model porous media. The results show the importance of wetting properties on the dynamics (**Figures 7 and 8**): For a water-wet (hydrophilic) porous medium, the drainage is rapid in the beginning and slower in the end, whereas in an oil-wet (hydrophobic) porous material, the drainage is much more regular (but slow). For hydrophilic porous media, the hydraulic continuity of the liquid phase allows for a flow through the liquid films that cover the porous material, whereas only bulk water displacement is observed for hydrophobic porous media. At the final stages of drainage, some water remains in the hydrophilic medium owing to capillary rise. However, a lot of water also is retained in the hydrophobic medium in a heterogeneous distribution of water pockets; the latter finding shows the importance of the hydraulic continuity of the water phase for an efficient removal of water. These results show the large impact of the wetting properties of porous media on the fluid transport through it, which is relevant, for

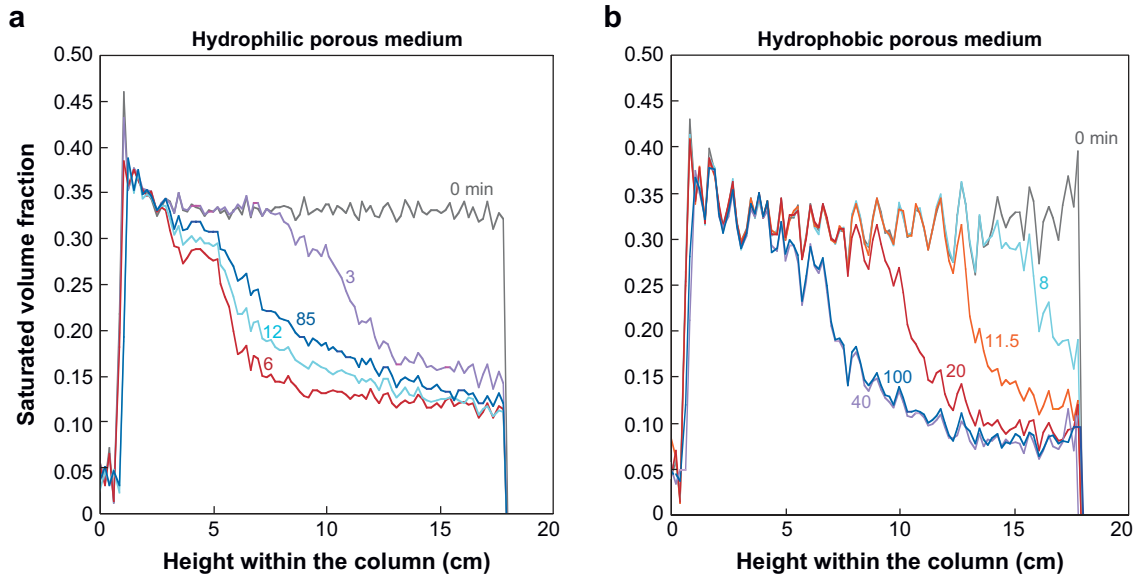


**Figure 7**

Magnetic resonance imaging profiles of the water content in a column during drainage; times indicated on the curves are in minutes (*a*) for the hydrophilic glass beads and (*b*) for the hydrophobic glass beads.

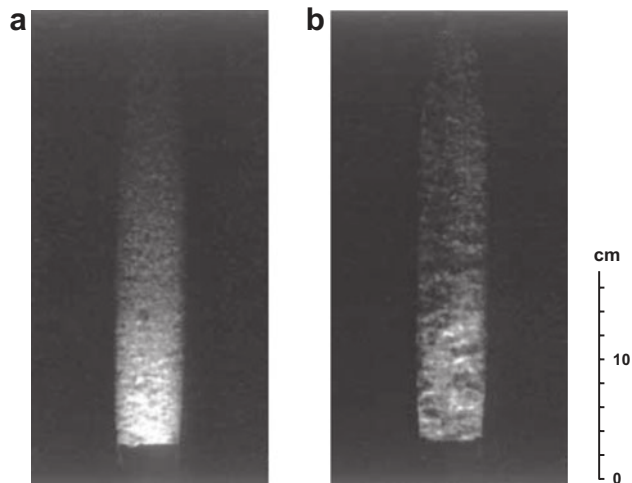


**Figure 8**

Magnetic resonance images of the water distribution within the column at the end of the drainage (*a*) for the hydrophilic glass beads and (*b*) the hydrophobic glass beads. The white color in the picture shows the presence of water in the column.

instance, for oil recovery, in which the wettability of the rocks has an influence on the oil recovery rate.

## 4. MRI RHEOLOGY

### 4.1. MRI Rheology of Complex Fluids

The flow behavior of complex fluids, such as polymer or surfactant solutions, is of both practical and fundamental interest (Larson 1999). The large length scales present in these systems, when compared to molecular dimensions, can lead to interactions between the flow field and the structure of the complex fluids. A structural change can affect the viscosity of the fluid and thus, in turn, modify the flow field; this coupling between structure and flow is in most cases responsible for the large difference in flow properties between complex fluids and normal (Newtonian) fluids. Traditional rheology, however, is blind in the sense that only macroscopic mechanical information is obtained in measurements. In the interpretation of such data, it is often implicitly or explicitly assumed that the flow of the material is homogeneous. However, this is often not the case in practice owing to the coupling between the flow and structure, and/or organization of complex fluids. In this section we consider a few examples that have recently been studied extensively using MRI to measure flow heterogeneity. The first one is a flow-induced phase transition in which a new phase with a different material viscosity appears when it is sheared sufficiently fast, leading to the coexistence of a low- and a high-viscosity state. The second example is the shear banding (localization) observed in yield stress fluids, and the third is flow-induced particle migration in (wet) granular materials.

In all these cases, MRI can be and has been used to obtain the local measurements of the flow and consequently of the flow properties, which is called MRI rheology. If the rheology is done in a Couette cell with an inner cylinder of radius  $R_i$ , and the corresponding stresses on the rotating inner cylinder  $\sigma_i$  are measured, the momentum balance equation gives the local stress at a radial distance  $r$  from the center of the MRI cell as  $\sigma = \sigma_i \frac{R_i^2}{r^2}$ . Then, with the MRI measurement of the velocity profile in the cell, the local shear rate follows from  $\dot{\gamma} = r \frac{\partial}{\partial r} \left( \frac{v_\theta}{r} \right)$ . The magnitude of the shear rate can thus be deduced from the velocity profile  $v_\theta(r)$ , and  $r$  can be eliminated from these two equations to deduce the constitutive equation of the fluid in simple shear, i.e., the relation between  $\sigma$  and  $\dot{\gamma}$ .

The common characteristic of the systems discussed below is that they all exhibit a stress plateau, i.e., a constant stress for a range of shear rates. Such plateaus have been observed for a variety of systems; the rheological interpretation of such plateaus is not straightforward, as, for instance, a stress plateau (a horizontal plateau) implies that for a given stress, several shear rates and consequently viscosities are possible. Such stress plateaus can have different origins, for surfactant systems principally observed in lamellar phases (Diat et al. 1993, Léon et al. 2000) and systems forming giant micelles (Berret et al. 1994, Cappelaere et al. 1997, Lerouge et al. 1998), but they are also observed for other complex fluids (McLeish & Ball 1986, Larson 1999, Panizza et al. 1995, Tordella 1969). The observations on some systems agree with

the hypothesis of a shear-induced coexistence (shear banding), whereas other invoke wall slip to account for the plateau. Most of this discussion is complicated because no detailed measurements of the velocity profiles in the moving liquid exist, making it difficult to assert what underlies such stress plateaus. In the past few years MRI has been used extensively to study this and has allowed for the detection of wall slip, for instance, in flowing foams and emulsions (Bertola et al. 2003), silicone oil-in-water emulsions, xanthan gum, and mayonnaise (Gibbs et al. 1996, Johns & Hollingsworth 2007, Rofe et al. 1996). Conversely, much effort has been put into the understanding of shear banding, which we discuss below.

## 4.2. Shear Banding in Surfactant Systems

One problem that has attracted much attention lately is the effect of shear on the flow and structure of surfactant solutions (Berret et al. 1994, Cappelaere et al. 1997, Diat et al. 1993, Hu et al. 1998, Léon et al. 2000, Lerouge et al. 1998, Oda et al. 1996, Spenley et al. 1993). Rheo-MRI has allowed for significant new insights into this problem. We focus here on shear-induced phase coexistence, which occurs most frequently in wormlike micellar surfactant solutions and is in general characterized by a plateau (vertical or horizontal) in the measured flow curves, i.e., of the stress as a function of the shear rate (Berret et al. 1994, Olmsted 1999). A proposed explanation is a shear-induced phase coexistence: A shear-induced phase transition occurs (Berret et al. 1994, Olmsted & Golbart 1990, Porte et al. 1997) at a certain shear rate, and the plateau signals a two-phase coexistence. The variation of the (average) shear rates is achieved if the proportion of the less viscous phase (which has the larger shear rate) grows, and the proportion of the more viscous phase diminishes. Researchers have tested this proposition using MRI (Fischer & Callaghan 1999, Lopez-Gonzalez et al. 2004, Mair & Callaghan 1996) and also light scattering (Salmon et al. 2003), ultrasound (Manneville et al. 2004), and particle imaging velocimetry (Mendez-Sanchez et al. 2003). To demonstrate MRI's potential in these problems, we discuss one specific example: Drappier et al.'s (2006) study of a system of wormlike micelles. In the rheology, imposing first the shear rate and plotting the shear stress as a function of the shear rate (**Figure 9**), they observed an almost horizontal plateau. During the plateau, the same shear stress  $\sigma$  is measured, for a shear rate between  $\dot{\gamma}_1 \approx 1 \text{ s}^{-1}$  and  $\dot{\gamma}_2 \approx 100 \text{ s}^{-1}$ . Consequently, the viscosity  $\eta = \frac{\sigma}{\dot{\gamma}}$  decreases during the plateau, and the system is strongly shear thinning.

The velocity profile in the gap measured by MRI using 2D phase-shift mapping (**Figure 10**) shows that on increasing the shear rate on the stress plateau, a highly sheared region progressively invades the gap. This region appears to correspond to the birefringent band; the larger part of the shear rate is concentrated in the new band, near the rotating cylinder, and we may conclude that the shear-induced phase has a lower viscosity. **Figure 10** also shows a clear discontinuity in slope in the profile, corresponding to the low- and high-shear band. Drappier et al. (2006) were able to locate the average position of the interface rather precisely, although large fluctuations in the interface position have been observed in similar systems (Becu et al. 2004, Holmes et al. 2003, Lopez-Gonzalez et al. 2004). **Figure 11** shows

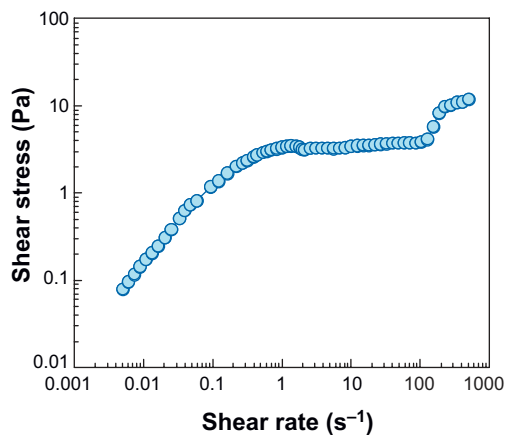


**Figure 9**  
Shear stress as a function of the shear rate for a wormlike micellar system measured in a Couette cell. Figure taken from Drappier et al. 2006.

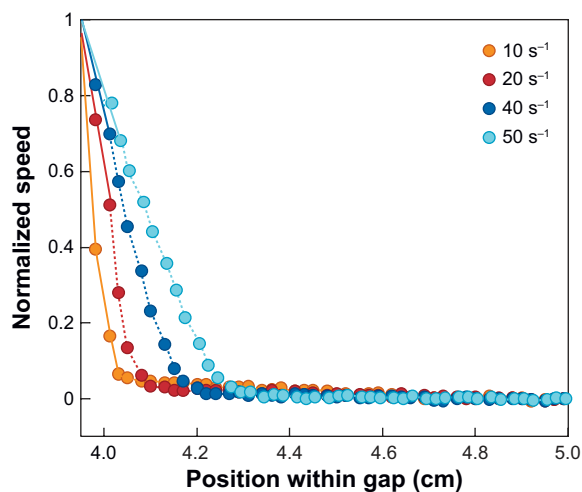


**Figure 10**  
Velocity profiles measured by magnetic resonance imaging for different imposed shear rates. Increasing the shear rate on the stress plateau causes a highly sheared region to progressively invade the gap (the gap is 1 cm). For each imposed shear rate, the velocity of the wall is denoted as  $v_w$ .

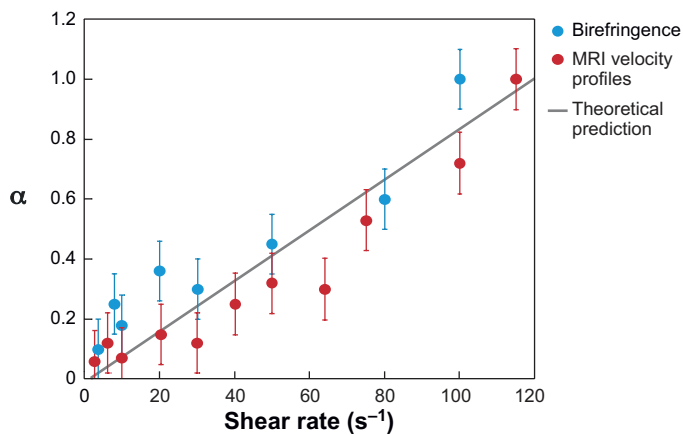


**Figure 11**  
Width of the shear band relative to the gap width from magnetic resonance imaging (MRI) velocity profiles compared with those measured using birefringence and to the theoretical prediction from a simple lever rule.

a comparison with the fraction of the gap occupied by the bands as a function of the macroscopic shear rate and shows that the proportion of the induced phase can be calculated by a simple lever rule:

$$\alpha = \frac{\gamma - \gamma_1}{\gamma_2 - \gamma_1}.$$

To quantify the shear bands, one can view the MRI measurements on these homogeneous fluids as agreeing with the rheology measurements. It seems reasonable to suppose that for the limited range of stresses and shear rates covered in a single experiment, the behavior of a homogeneous fluid can be approximated by a power-law shear thinning behavior:  $\eta = k\gamma^{n-1}$ , with  $\eta$  the viscosity,  $k$  a constant,  $\gamma$  the shear rate, and  $n$  the power-law exponent. If this is done, the Stokes equation gives the following velocity profile:

$$v_\theta(r) = \omega r \frac{(R_2/r)^{2/n} - 1}{(R_2/R_1)^{2/n} - 1},$$

with  $\omega$  the angular velocity of the inner cylinder;  $R_1$  and  $R_2$  the radii of inner and outer cylinder, respectively; and  $r$  the position in the gap from the axis of the inner cylinder.

Fitting, for instance, the velocity profile in the low-shear band from the MRI, one finds  $n = 0.29$ , in agreement with the flow curve obtained using the rheometer before the stress plateau that gives  $n = 0.32$ . From the comparison between the local MRI measurements with the macroscopic flow curve, it follows that all the experimental observations agree with the simple idea of a shear-induced transition between a high- and a low-viscosity phase; the detailed analysis of the velocity profiles allows for the conclusion that the viscosities of the coexisting phases are those of the homogeneous fluids that exist before and after the stress plateau.

### 4.3. MRI Rheology of Yield Stress Fluids

Yield stress fluids are materials made of a high concentration of small elements (colloidal particles, bubbles, droplets, microgel beads, etc.) immersed in an interstitial liquid. As such their rheological behavior is not simple (i.e., they are non-Newtonian fluids), which finds its origin in their jammed structure: the continuous network of interactions between elements throughout the sample. Such materials are said to have a yield stress; i.e., they are solid as long as the applied stress is smaller than a critical value (the yield stress,  $\sigma_c$ ) and liquid otherwise. The yield stress corresponds to the minimum stress needed to break the network of interactions. Moreover, they are often thixotropic; i.e., their apparent viscosity depends on the flow history. Typically, this takes the form of an increase of the yield stress at rest and a decrease of the viscosity in the liquid regime after flow start. These materials may also easily develop slip along a smooth solid wall as a result of some particle depletion at the approach of the wall. The yielding, thixotropy, and wall slip are usually inferred from macroscopic conventional rheometry, so MRI velocimetry can provide direct evidence and measurements of these phenomena within pastes, which are generally nontransparent materials.

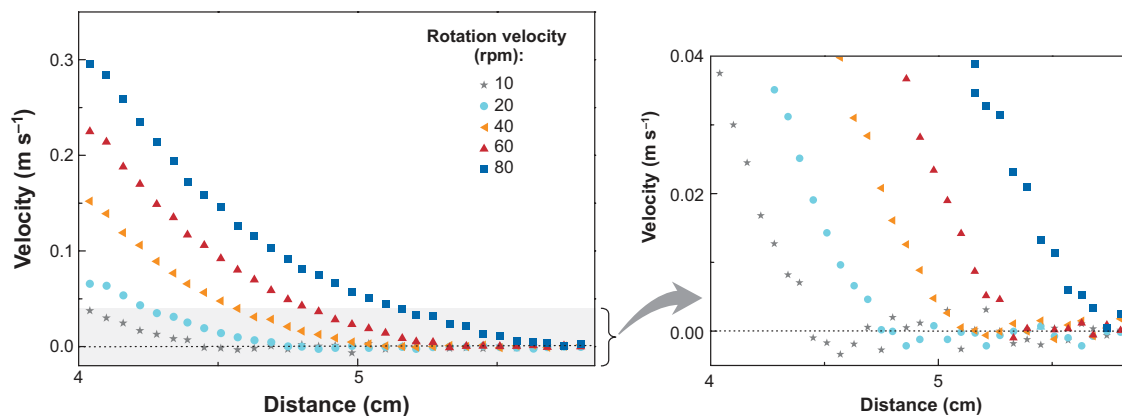


**Figure 12**

Magnetic resonance imaging velocity profiles using 2D phase-shift mapping for a foam (Gilette foamy regular) in a Couette cell.

The yielding behavior implies that as soon as the stress is not homogeneous, solid and liquid regions can coexist within the sample. For example, in the simple shear flow inside a coaxial cylinder (Couette) rheometer the shear stress decreases as the square of the distance ( $r$ ) from the central axis:  $\sigma = \sigma_1 \frac{R_1^2}{r^2}$ . It follows that when  $\sigma_1 < \sigma_c (R_2/R_1)^2$ , the material is in its liquid regime up to the critical distance  $r_c = R_1 \sqrt{\sigma/\sigma_c}$ , so the thickness of the sheared region is  $e = R_1(\sqrt{\sigma/\sigma_c} - 1)$ . Beyond this distance, the material remains in its solid regime. Obviously when the torque or the rotation velocity of the inner cylinder ( $\Omega$ ) increases, the sheared region decreases (see **Figure 12**). MRI velocimetry makes it possible to observe directly this effect with typical pasty materials (Callaghan 1999, Ragouillaux et al. 2006, Raynaud et al. 2002, Rodts et al. 2005, Wassenius & Callaghan 2005).

Also the behavior of the material beyond the yield stress is still not that of a Newtonian fluid; i.e.,  $\sigma - \sigma_c$  is not proportional to the shear rate  $\dot{\gamma}$ . This implies that the slope of the velocity profile in a Couette rheometer may vary significantly in the sheared region. This was effectively observed by MRI (see **Figure 12** and above references). In that case, one may even deduce the behavior of the material from the velocity profile in the sheared region as explained above; however, the range of variation of the shear stress from the solid-liquid interface to the inner cylinder is generally rather short, so the constitutive law is only measured over a limited range of stresses.

MRI velocimetry made it possible to better understand some peculiar effects occurring at the interface between the solid and the liquid regions. Indeed it is usually considered that the shear rate decreases to zero at the approach of the yield stress ( $\dot{\gamma} \rightarrow 0$  when  $\sigma \rightarrow \sigma_c$ ). In practice, researchers observed an abrupt change of the slope of the velocity profile at the solid-liquid interface (Coussot et al. 2002a), indicating that  $\dot{\gamma} \rightarrow \dot{\gamma}_c$  when  $\tau \rightarrow \tau_c$ , with  $\dot{\gamma}_c \neq 0$  (Bonn et al. 2002, Jarny et al.



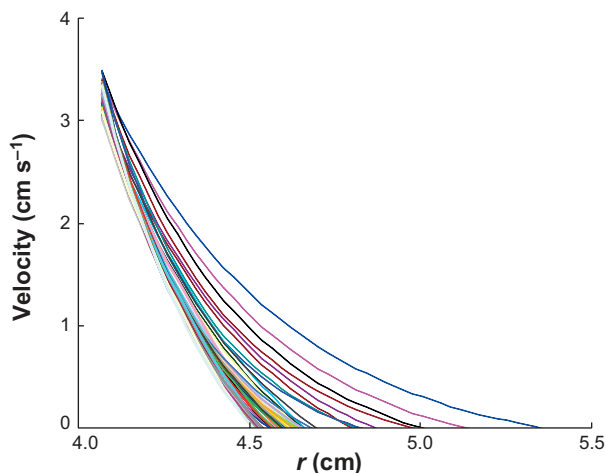


**Figure 13**

Magnetic resonance imaging velocity profiles for a bentonite suspension (3.2%) during transient tests, here represented, for the sake of clarity, by exponential functions fitted to data in the sheared region: sudden change from 60 to 10 rpm (increasing time from right to left). The delay between two successive velocity profiles is 25.6 s, and the steady state is reached after a time of the order of 600 s. Data taken from Raynaud et al. 2002.

2005, Ragouillaux et al. 2006, Rodts et al. 2005). Such an effect had been suggested by some conventional rheometry works (Coussot et al. 2002b), but MRI definitely confirmed its existence and provides an accurate technique for determining this new rheological parameter ( $\dot{\gamma}_c$ ). A particular consequence of this effect is that the material cannot support a steady shear at a rate below  $\dot{\gamma}_c$ , so shear-banding should occur even in cone and plate geometry, as observed for a bentonite suspension (Coussot et al. 2002a).

Because the apparent viscosity, and in particular the yield stress, can depend on the flow history, we can expect that the velocity profile determined by MRI velocimetry will evolve in time. This is typically the effect observed with strongly thixotropic suspensions (see **Figure 13**): The sheared thickness in steady state decreases with the time of rest before flow (for the same value of  $\Omega$ ). Also, as a result of viscosity variations in time, in transient flows we can expect that the shape of the velocity profile and/or the position of the solid-liquid interface will evolve in time (Raynaud et al. 2002). However, for now there is no straightforward technique for interpreting such data in rheological terms. This does not reflect a weakness of MRI, which on the contrary provides a huge set of data from any such experiment, but more reflects the absence of general rheological tools for describing in a general way the thixotropy of complex fluids. Raynaud et al. (2002) attempted to interpret this and concluded that the apparent thixotropic behavior of the paste is mainly controlled by the displacement of the solid-liquid interface, whereas the apparent viscosity in the liquid phase does not change much. Also the predictions of a simple thixotropy model have been compared with these data (Roussel et al. 2004).

#### 4.4. MRI Rheology of Wet Granular Materials

The seemingly simple question of whether a constitutive equation can be defined for granular systems in general does not appear to have a simple answer (GDR MiDi 2004, Jaeger et al. 1996, Mueth et al. 2000), despite the necessity, for a large number of applications, of predicting the resistance to flow. Because of the volume conservation that is not necessarily present for dry granular materials, perhaps the simplest example of granular flow is that of wet granular materials (i.e., pastes), which are of crucial importance in industrial and civil engineering, and in geophysics (Herminghaus 2005). For wet granular materials, from the comparison between global (rheological) measurements of the viscosity and local measurements using velocity profiles measured in a Couette cell with an MRI scanner, researchers concluded that there is no simple constitutive equation relating shear stress to shear rate only, as may be observed in **Figure 14** from the difference in viscosities deduced from local (MRI) and global measurements (Huang et al. 2005).

This conclusion was attributed to the migration of particles, another phenomenon that can be studied by MRI. From the local MRI rheology, one can calculate the viscosity variation in the gap, as is shown in **Figure 15**. Using MRI to measure the gradient in particle density, researchers found that, owing to the flow, the material is dilated where it flows rapidly and compacted where the flow is slow (Ovarlez et al. 2006). This results in the local variation of the viscosity.

Such shear-induced particle migration has been studied mainly in conduits and Couette rheometers (Abbott et al. 1991, Altobelli et al. 1991, Chow et al. 1994, Corbett et al. 1995, Götz et al. 2001, Graham et al. 1991, Sinton & Chow 1991) but may be not enough systematically for a full understanding of the basic processes of migration. Independent of the mechanism of migration, the measurement of the density profile for the granular paste showed that the particle volume fraction increases linearly with increasing distance from the moving inner cylinder, which qualitatively confirms that the viscosity varies within the gap owing to a flow-induced density

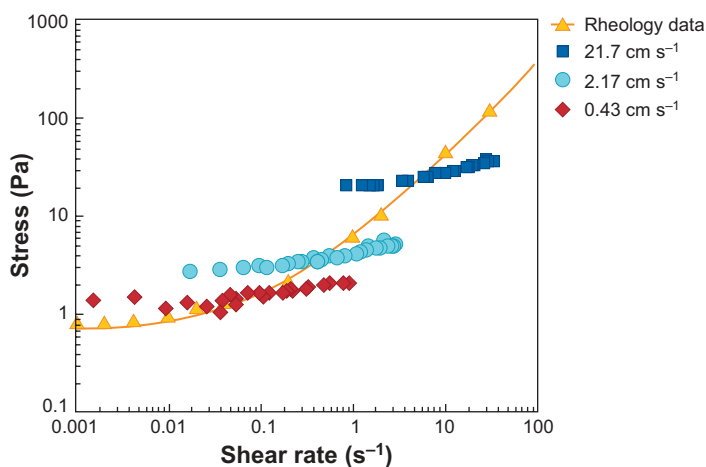
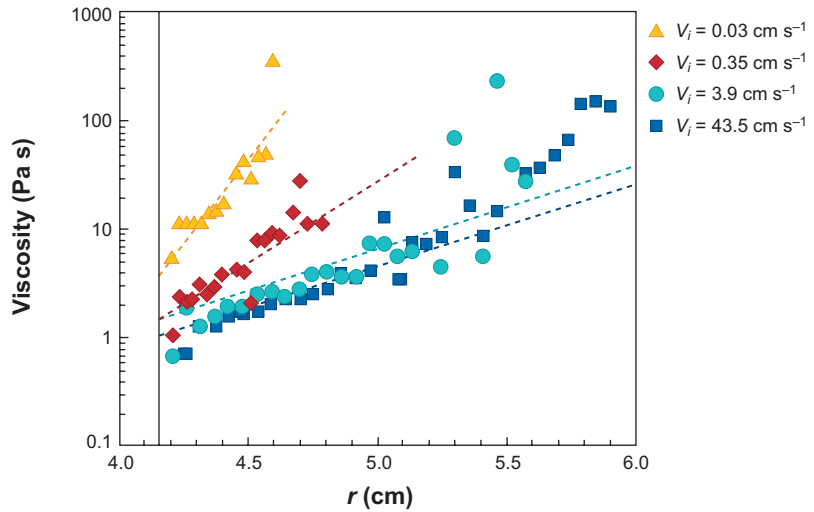


**Figure 14**

The rheology of concentrated suspensions (solid volume fraction approximately 60%) of polystyrene particles in a Newtonian fluid studied by conventional rheology and magnetic resonance imaging.

**Figure 15**

Variation of the viscosity in a Couette cell, as deduced from the magnetic resonance imaging velocity profile.



gradient (Abbott et al. 1991, Leighton & Acrivos 1987, Phillips et al. 1992). This in turn allows the definition of a constitutive equation for the wet granular material. It follows that the flow of the dense suspension is governed by the flow curve equation  $\sigma = \eta(\varphi) \dot{\gamma}$ . The viscosity  $\eta(\varphi)$  can then be measured independently in rheology measurements. If all these data are taken together, we can show not only that the MRI-rheology data are consistent with themselves (Ovarlez et al. 2006), but also that agreement with macroscopic rheology can be obtained (N. Huang & D. Bonn, unpublished manuscript).

## 5. MRI FLOW MEASUREMENTS IN CARDIOVASCULAR MEDICINE

In past decades, the application of MRI techniques for a more accurate quantification of blood flow rates through vessels, heart valves, and conduits has greatly enhanced our knowledge about the distribution of blood volume and the consequences of cardiovascular overload in a number of pathological conditions (Taylor & Draney 2004). As such, it has guided medical intervention in a number of cardiovascular diseases. Although Doppler echocardiography is still predominantly used to study blood flow dynamics in the clinical setting, this technique lacks the ability to calculate spatial average velocity and volume flow in spatially nonuniform pulsatile flow profiles, common in the heart and great vessels, and is therefore considered less suited to quantify blood flow *in vivo*. Among the most important applications in cardiovascular medicine are the diagnoses of heart failure, heart valve disease, and vascular disease.

Heart failure may be caused by inborn unfavorable anatomy (congenital heart disease), heart muscle disease (inborn or as a result from heart valve/vascular disease), or heart valve disease. Although echocardiography is generally sufficient to determine the cause of heart failure, MRI is often helpful in the assessment of the severity of disease and in guiding therapy. Other than with echocardiography, there are no

anatomical limitations in finding the correct imaging planes. By measuring volume flow through the aorta, one can measure cardiac output, which is a measure of cardiac performance. In addition, the assessment of inflow through the valves yields the characteristics of ventricular filling, a disturbance generally considered an early stage of heart failure. Investigators have recently shown that it can even be the sole cause of decreased cardiac performance in some cases (Rademakers & Bogaert 2006), and MRI assessment of this is thus clinically relevant.

MRI is also the only in vivo modality capable of the quantification of leakage and obstruction of the heart valves, which is of great clinical importance. **Figure 16** shows an example of a high-velocity jet of blood emerging from a narrowed heart valve. The quantitative assessment of valvular obstruction (stenosis) is generally performed

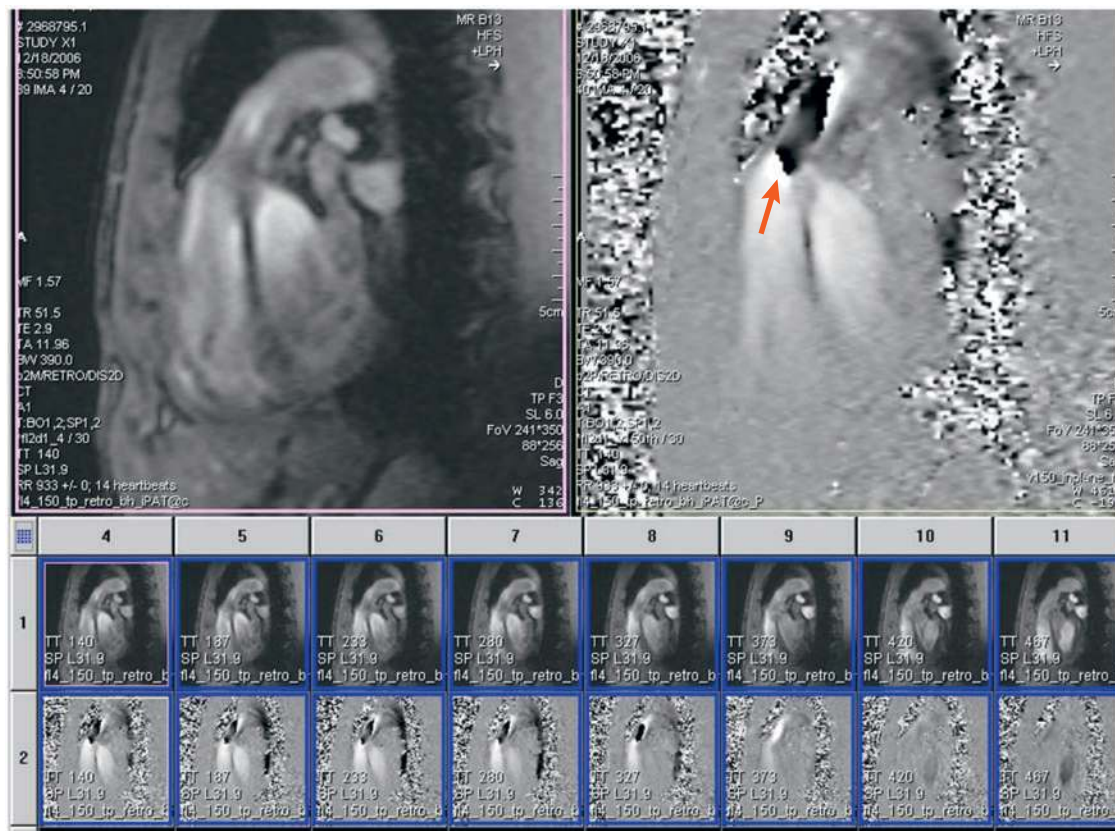
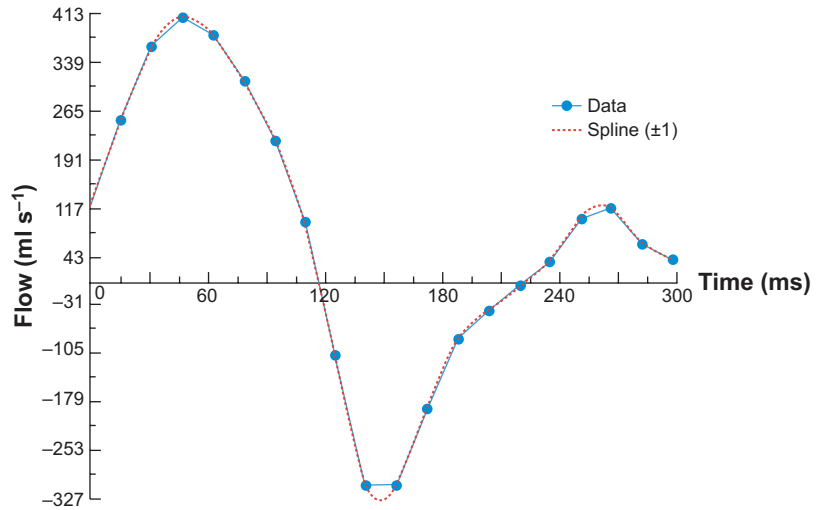


**Figure 16**

Assessment of flow through a narrowed heart valve (stenosis) by phase-contrast velocity mapping. (*Left panel*) The modulus (direct) image of the heart. (*Right panel*) A high velocity jet above the pulmonary valve can be seen (*arrow*) on the phase image. The small figures (*bottom panel*) show 8 of the 30 frames from the cardiac cycle; i.e., approximately 30 frames correspond to one heartbeat.

**Figure 17**

Volume flow through the incompetent pulmonary valve showing severe leakage. A positive flow rate corresponds to blood going through in the right direction; negative values correspond to the wrong direction.



by evaluating the pressures on each side of the valve from the Bernoulli equation,  $p = \frac{1}{2}\rho v^2$ , where  $v$  is the maximum velocity distal from the valve. In this case, MRI can yield a reliable velocity measurement and thus allows for a quantitative assessment of the problem. **Figure 17** shows the quantitative measurement of the flow through the heart valve, and severe leakage of the valve is concluded from the negative part of the flow curve; the latter means that blood flows back through the valve, which results in volume overload of the heart.

On a research level, flow patterns in the heart investigated by MRI have allowed researchers studying implanted artificial heart valves to direct the development of new artificial valves with better hemodynamic profiles (Kozerke et al. 2001, Rahimtoola 2006). In addition, although spatial resolution is limited with current MRI scanners, efforts have been made to measure flow in coronary arteries and bypass grafts by MRI, to assess the severity of coronary obstructions (Langerak et al. 2002). This application is still in a research phase but may evolve into a useful tool in the diagnosis and treatment of coronary artery disease. By applying velocity gradients in three directions, one can image 3D contraction patterns of the heart muscle, allowing the isolation of defective regions (Jung et al. 2006). Flow measurements in the great arteries facilitate the assessment of pulse wave velocity, a measure of arterial elasticity, which is of clinical importance in heart failure and degenerative vascular disease (Nollen et al. 2004).

MRI is also useful in the diagnosis and treatment of congenital (inborn) heart disease (Sahn & Vick 2001). One of the major problems here is the quantification of intra- and extracardiac shunts (a shunt is a hole or faulty connection in the blood flow circuit, allowing blood to bypass the normal circuit), which has always been a quite elaborate invasive investigation. With MRI, two flow measurements through the aorta and pulmonary artery will do the job. In the congenital narrowing of the aorta (aortic coarctation), the severity of obstruction is indicated by the extent of collateral

circulation. Again, only two flow measurements through the aorta are necessary, one before the obstruction and one at the level of the diaphragm. Flow measurements in implanted conduits and pulmonary arteries may reveal obstruction, not detectable by echocardiography.

## 6. CONCLUSION AND PERSPECTIVES

In this article, we briefly review some of the most important and/or spectacular applications of magnetic resonance imaging to study flow: multiphase flows, the MRI rheology of complex fluid flows, and blood flows in the human body. In all these cases, MRI offers very good 3D flow imaging possibilities with a high precision on the flow speed, a reasonable spatial resolution, and a high data acquisition rate; the above examples on cardiac MRI imaging are especially impressive in this respect. Previous reviews have covered in a quasi-exhaustive way all possibilities offered for different fields such as chemical engineering, fluid mechanics, and fluid transport in porous media (Callaghan 1999, Fukushima 1999, Stapf & Han 2006). However, in spite of all the possibilities for the use of MRI, the gap between what MRI can potentially do and what MRI methods are routinely used for in fluid mechanics is still large, and the field is therefore open to many more applications in fluid mechanics.

## DISCLOSURE STATEMENT

The authors are not aware of any biases that might be perceived as affecting the objectivity of this review.

## LITERATURE CITED

- Abbott JR, Tetlow N, Graham AL, Altobelli SA, Fukushima E, et al. 1991. Experimental observations of particle migration in concentrated suspensions: Couette flow. *J. Rheol.* 35:773–95
- Altobelli SA, Givler RC, Fukushima E. 1991. Velocity and concentration measurements of suspensions by nuclear magnetic resonance imaging. *J. Rheol.* 35:721–34
- Becu L, Manneville S, Colin A. 2004. Spatiotemporal dynamics of wormlike micelles under shear. *Phys. Rev. Lett.* 93:018301
- Berret JF, Roux DC, Porte G. 1994. Isotropic-to-nematic transition in wormlike micelles under shear. *J. Phys. II* 4:1261–79
- Bertola V, Bertrand F, Tabuteau H, Bonn D, Coussot P. 2003. Wall slip and yielding in pasty materials. *J. Rheol.* 47:1211–26
- Bonn D, Coussot P, Huynh HT, Bertrand F, Debregeas G. 2002. Rheology of soft-glassy materials. *Europhys. Lett.* 59:786–92
- Callaghan PT. 1999. Rheo-NMR: nuclear magnetic resonance and the rheology of complex fluids. *Rep. Prog. Phys.* 62:599–670
- Cappelaere E, Berret JF, Decrupe JP, Cressely R, Lindner P. 1997. Rheology, birefringence, and small-angle neutron scattering in a charged micellar system: evidence of a shear-induced phase transition. *Phys. Rev. E* 56:1869–78

- Chow AW, Sinton SW, Iwamiya JH, Stephens TS. 1994. Shear-induced particle migration in Couette and parallel-plate viscometers: NMR imaging and stress measurements. *Phys. Fluids* 6:2561–76
- Corbett AM, Philips RJ, Kauten RJ, McCarthy KL. 1995. Magnetic resonance imaging of concentration and velocity profiles of pure fluids and solid suspensions in rotating geometries. *J. Rheol.* 39:907–24
- Coussot P, Nguyen QD, Huynh HT, Bonn D. 2002a. Avalanche behavior in yield stress fluids. *Phys. Rev. Lett.* 88:175501
- Coussot P, Raynaud JS, Bertrand F, Moucheron P, Guilbaud JP, et al. 2002b. Coexistence of liquid and solid phases in flowing soft-glassy materials. *Phys. Rev. Lett.* 88:218301
- Diat O, Roux D, Nallet F. 1993. Effect of shear on a lyotropic lamellar phase. *J. Phys. II* 3:1427–52
- Drappier J, Bonn D, Meunier J, Lerouge S, Decruppe J-P, Bertrand F. 2006. Correlation between birefringent bands and shear bands in surfactant solutions. *J. Stat. Mech.: Theory Exp.* 2006:P04003
- Dumoulin CL, Souza SP, Walker MF, Wagle W. 1989. Three-dimensional phase-contrast angiography. *Magn. Res. Med.* 9:139–49
- Fischer E, Callaghan PT. 1999. Shear banding and the isotropic-to-nematic transition in wormlike micelles. *Phys. Rev. E* 64:011501
- Fukushima E. 1999. Nuclear magnetic resonance as a tool to study flow. *Annu. Rev. Fluid Mech.* 31:95–123
- GDR MiDi. 2004. On dense granular flows. *Eur. Phys. J. E* 14:341–65
- Gibbs SJ, James KL, Hall LD, Haycock DE, Frith WJ, Ablett S. 1996. Rheometry and detection of apparent wall slip for Poiseuille flow of polymer solutions and particulate dispersions by nuclear magnetic resonance velocimetry. *J. Rheol.* 40:425–40
- Götz J, Kreibich W, Peciar M, Buggisch H. 2001. MRI of Couette experiments in a newly developed shear device: suitable for pastes and concentrated suspensions. *J. Non-Newton. Fluid Mech.* 98:117–39
- Götz J, Zick K. 2003. Local velocity and concentration of the single components in water/oil mixtures monitored by means of MRI flow experiments in steady tube flow. *Chem. Eng. Technol.* 26:59–68
- Graham AL, Altobelli SA, Fukushima E, Mondy LA, Stephens TS. 1991. Note: NMR imaging of shear-induced diffusion and structure in concentrated suspensions undergoing Couette flow. *J. Rheol.* 35:191–201
- Hall ARW. 1997. Flow pattern in three-phase gas flows of oil, water and gas. *Proc. 8th Int. Conf. Multiph. '97, Cannes, France*. Cranfield, UK: BHR Group
- Herminghaus S. 2005. Dynamics of wet granular matter. *Adv. Phys.* 54:221–61
- Holmes WM, Lopez-Gonzalez MR, Callaghan PT. 2003. Fluctuations in shear-banded flow seen by NMR velocimetry. *Europhys. Lett.* 64:274–80
- Hu Y, Boltenhagen P, Pine DJ. 1998. Shear thickening in low-concentration solutions of wormlike micelles. I. Direct visualization of transient behavior and phase transitions. *J. Rheol.* 79:1185–208
- Huang N, Ovarlez G, Bertrand F, Rodts S, Coussot P, Bonn D. 2005. Flow of wet granular materials. *Phys. Rev. Lett.* 94:028301

- Hundley WG, Li HF, Willard JE, Landau C, Lange RA, et al. 1995. Magnetic resonance imaging assessment of the severity of mitral regurgitation: comparison with invasive techniques. *Circulation* 92:1151–58
- Jaeger HM, Nagel SR, Behringer RP. 1996. Granular solids, liquids, and gases. *Rev. Mod. Phys.* 68:1259–73
- Jarny S, Roussel N, Rodts S, Le Roy R, Coussot P. 2005. Rheological behavior of cement pastes from MRI velocimetry. *Concr. Cem. Res.* 35:1873–81
- Johns ML, Hollingsworth KG. 2007. Characterisation of emulsion systems using NMR and MRI. *Prog. Nucl. Magn. Res. Spectrosc.* 50:51–70
- Jung B, Foll D, Bottler P, Petersen S, Hennig J, Markl M. 2006. Detailed analysis of myocardial motion in volunteers and patients using high-temporal-resolution MR tissue phase mapping. *J. Magn. Reson. Imaging* 24:1033–39
- Kozerke S, Hasenkam JM, Nygaard H, Paulsen PK, Pedersen EM, Boesiger P. 2001. Heart motion-adapted MR velocity mapping of blood velocity distribution downstream of aortic valve prostheses: initial experience. *Radiology* 218:548–55
- Langerak SE, Kunz P, Vliegen HW, Jukema JW, Zwinderman AH, et al. 2002. MR flow mapping in coronary artery bypass grafts: a validation study with Doppler flow measurements. *Radiology* 222:127–35
- Larson RG. 1999. *The Structure and Rheology of Complex Fluids*. New York: Oxford Univ. Press
- Le Gall F, Pascal-Ribot S, Leblond J. 2001. Nuclear magnetic resonance measurements of fluctuations in air-water two-phase flow: pipe flow with and without “disturbing” section. *Phys. Fluids* 13:1118–29
- Leighton D, Acrivos A. 1987. The shear-induced migration of particles in concentrated suspensions. *J. Fluid Mech.* 181:415–39
- Léon A, Bonn D, Meunier J. 2000. Coupling between flow and structure for a lamellar surfactant phase. *Phys. Rev. Lett.* 84:1335–38
- Lerouge S, Decruppe JP, Humbert C. 1998. Shear banding in a micellar solution under transient flow. *Phys. Rev. Lett.* 81:5457–60
- Lopez-Gonzalez MR, Holmes WM, Callaghan PT, Photinos PJ. 2004. Shear banding fluctuations and nematic order in wormlike micelles. *Phys. Rev. Lett.* 93:268302
- Mair RW, Callaghan PT. 1996. Observation of shear banding in wormlike micelles by NMR velocimetry imaging. *Europhys. Lett.* 36:719–24
- Manneville S, Salmon JB, Colin A. 2004. A spatio-temporal study of rheo-oscillations in a sheared lamellar phase using ultrasound. *Eur. Phys. J. E* 13:197–22
- Mantle MD, Sederman AJ. 2003. Dynamic MRI in chemical process and reaction engineering. *Prog. Nucl. Magn. Res. Spectrosc.* 43:3–60
- McLeish TCB, Ball RC. 1986. A molecular approach to the spurt effect in polymer melt flow. *J. Polym. Sci. Polym. Phys. Ed.* 24:1735–45
- Mendez-Sanchez AF, Perez-Gonzalez J, de Vargas L, Castrejon-Pita JR, Castrejon-Pita AA, Huelsz G. 2003. Particle image velocimetry of the unstable capillary flow of a micellar solution. *J. Rheol.* 47:1455–66
- Merboldt KD, Hanicke EW, Frahm J. 1986. Flow NMR imaging using stimulated echoes. *J. Magn. Reson.* 67:336–41



- Moser KW, Raguin LG, Harris A, Morris HD, Georgiadis J, et al. 2000. Visualisation of Taylor-Couette and spiral Poiseuille flows using a snapshot FLASH spatial tagging sequence. *Magn. Res. Imaging* 18:199–207
- Mueth DM, Debregeas GF, Karczmar GS, Eng PJ, Nagel SR, Jaeger HM. 2000. Signatures of granular microstructure in dense shear flows. *Nature* 406:385–89
- Muller CR, Holland DJ, Davidson JF, Dennis JS, Gladden LF, et al. 2007. Rapid two-dimensional imaging of bubbles and slugs in a three-dimensional, gas-solid, two-phase flow system using ultrafast magnetic resonance. *Phys. Rev. E* 75:020302
- Nollen GJ, Groenink M, Tijssen JG, Van Der Wall EE, Mulder BJ. 2004. Aortic stiffness and diameter predict progressive aortic dilatation in patients with Marfan syndrome. *Eur. Heart J.* 25:1146–52
- Oda R, Panizza P, Schmutz M, Lequeux F. 1996. Direct evidence of the shear-induced structure of wormlike micelles: Gemini surfactant 12–2–12. *Langmuir* 13:6407–12
- Olmsted PD. 1999. Two-state shear diagrams for complex fluids in shear flow. *Europhys. Lett.* 48:339–45
- Olmsted PD, Golbart PM. 1990. Theory of the nonequilibrium phase transition for nematic liquid crystal under shear flow. *Phys. Rev. A* 41:4578–81
- Ovarlez G, Bertrand F, Rodts S. 2006. Local determination of the constitutive law of a dense suspension of noncolloidal particles through MRI. *J. Rheol.* 50:259–92
- Panizza P, Archambault P, Roux D. 1995. Effects of shear on the smectic A phase of thermotropic liquid crystals. *J. Phys. II* 5:303–11
- Pelc NJ, Herfkens RJ, Shimakawa A, Enzmann DR. 1991. Phase contrast cine magnetic resonance imaging. *Magn. Res. Q.* 7:229–54
- Petrella JR, Provenzale JM. 2000. MR perfusion imaging of the brain: techniques and applications. *AJR Am. J. Roentgenol.* 175:207–19
- Phillips RJ, Armstrong RC, Brown RA, Graham AL, Abbott JR. 1992. A constitutive equation for concentrated suspensions that accounts for shear-induced particle migration. *Phys. Fluids A* 4:30–40
- Porte G, Berret JF, Harden J. 1997. Inhomogeneous flows of complex fluids: mechanical instability versus non-equilibrium phase transition. *J. Phys. II* 7:459–72
- Rademakers FE, Bogaert J. 2006. Cardiac dysfunction in heart failure with normal ejection fraction: MRI measurements. *Prog. Cardiovasc. Dis.* 49:215–27
- Ragouilliaux A, Herzhaft B, Bertrand F, Coussot P. 2006. Flow instability and shear localization in a drilling mud. *Rheol. Acta* 46:261–71
- Rahimtoola SH. 2006. The year in valvular heart disease. *J. Am. Coll. Cardiol.* 47:427–39
- Raynaud JS, Moucheron P, Baudez JC, Bertrand F, Guilbaud JP, Coussot P. 2002. Direct determination by NMR of the thixotropic and yielding behavior of suspensions. *J. Rheol.* 46:709–32
- Rodts S, Baudez JC, Coussot P. 2005. From discrete to continuum flow in foams. *Europhys. Lett.* 69:636–42
- Rodts S, Bertrand F, Jarny S, Poullain P, Moucheron P. 2004. Développements récents dans l'application de l'IRM à la rhéologie et à la mécanique des fluides. *C.R. Chim.* 7:275–82

- Rofe CJ, de Vargas L, Perez-González J, Lambert RK, Callaghan PT. 1996. Nuclear magnetic resonance imaging of apparent slip effects in xanthan solutions. *J. Rheol.* 40:1115–28
- Roussel N, Le Roy R, Coussot P. 2004. Test of a thixotropy model by comparison with local and macroscopic flow properties. *J. Non-Newton. Fluid Mech.* 117:85–95
- Sahn DJ, Vick GW III. 2001. Review of new techniques in echocardiography and magnetic resonance imaging as applied to patients with congenital heart disease. *Heart* 86(Suppl. 2):II41–53
- Salmon JB, Colin A, Manneville S. 2003. Velocity profiles in shear-banding wormlike micelles. *Phys. Rev. Lett.* 90:228303
- Shahidzadeh-Bonn N, Tournie A, Bichon S, Vie P, Rodts S, et al. 2004. Effect of wetting on the dynamics of drainage in porous media. *Transp. Porous Media* 56:209–24
- Singer JR. 1959. Blood flow rates by nuclear magnetic resonance measurements. *Science* 130:1652–53
- Singer JR, Crooks LE. 1983. Nuclear magnetic resonance blood flow measurements in the human brain. *Science* 221:654–56
- Sinton SW, Chow AW. 1991. NMR flow imaging of fluids and solids suspensions in Poiseuille flow. *J. Rheol.* 35:735–71
- Spenley NA, Cates ME, McLeish TCB. 1993. Nonlinear rheology of wormlike micelles. *Phys. Rev. Lett.* 71:939–42
- Stapf S, Han S, eds. 2006. *NMR Imaging in Chemical Engineering*. Weinheim: Wiley-VCH
- Taylor CA, Draney M. 2004. Experimental and computational methods in cardiovascular fluid mechanics. *Annu. Rev. Fluid Mech.* 36:197–231
- Tordella JP. 1969. *Rheology, Theory and Applications*, ed. FR Eirich. New York: Academic
- Wassenius H, Callaghan PT. 2005. NMR velocimetry studies of the steady-shear rheology of a concentrated hard-sphere colloidal system. *Eur. Phys. J. E* 18:69–84
- Zerhouni EA, Parish DM, Rogers WJ, Yang A, Shapiro EP. 1988. Human heart tagging with MR imaging: a method for non-invasive assessment of myocardial motion. *Radiology* 169:59–74



# Contents

Flows of Dense Granular Media <i>Yoël Forterre and Olivier Pouliquen</i> .....	1
Magnetohydrodynamic Turbulence at Low Magnetic Reynolds Number <i>Bernard Knaepen and René Moreau</i> .....	25
Numerical Simulation of Dense Gas-Solid Fluidized Beds: A Multiscale Modeling Strategy <i>M.A. van der Hoef, M. van Sint Annaland, N.G. Deen, and J.A.M. Kuipers</i> .....	47
Tsunami Simulations <i>Galen R. Gislér</i> .....	71
Sea Ice Rheology <i>Daniel L. Feltham</i> .....	91
Control of Flow Over a Bluff Body <i>Haecheon Choi, Woo-Pyung Jeon, and Jinsung Kim</i> .....	113
Effects of Wind on Plants <i>Emmanuel de Langre</i> .....	141
Density Stratification, Turbulence, but How Much Mixing? <i>G.N. Ivey, K.B. Winters, and J.R. Koseff</i> .....	169
Horizontal Convection <i>Graham O. Hughes and Ross W. Griffiths</i> .....	185
Some Applications of Magnetic Resonance Imaging in Fluid Mechanics: Complex Flows and Complex Fluids <i>Daniel Bonn, Stéphane Rodts, Maarten Groenink, Salima Rafai, Noushine Shahidzadeh-Bonn, and Philippe Coussot</i> .....	209
Mechanics and Prediction of Turbulent Drag Reduction with Polymer Additives <i>Christopher M. White and M. Godfrey Mungal</i> .....	235
High-Speed Imaging of Drops and Bubbles <i>S.T. Thoroddsen, T.G. Etoh, and K. Takebara</i> .....	257

Oceanic Rogue Waves <i>Kristian Dysthe, Harald E. Krogstad, and Peter Müller</i> .....	287
Transport and Deposition of Particles in Turbulent and Laminar Flow <i>Abhijit Guha</i> .....	311
Modeling Primary Atomization <i>Mikhael Gorokhovski and Marcus Herrmann</i> .....	343
Blood Flow in End-to-Side Anastomoses <i>Francis Loth, Paul F. Fischer, and Hisbam S. Bassiouny</i> .....	367
Applications of Acoustics and Cavitation to Noninvasive Therapy and Drug Delivery <i>Constantin C. Coussios and Ronald A. Roy</i> .....	395

## Indexes

Subject Index .....	421
Cumulative Index of Contributing Authors, Volumes 1–40 .....	431
Cumulative Index of Chapter Titles, Volumes 1–40 .....	439

## Errata

An online log of corrections to *Annual Review of Fluid Mechanics* articles may be found at <http://fluid.annualreviews.org/errata.shtml>